JOURNAL OF MAGNETIC RESONANCE **128,** 161–171 (1997)
ARTICLE NO. MN971220

# Dynamic Contrast-Enhanced Imaging and Analysis at High Spatial Resolution of MCF7 Human Breast Tumors

Edna Furman-Haran, Dov Grobgeld, and Hadassa Degani[1]

*Department of Biological Regulation, Weizmann Institute of Science, 76100 Rehovot, Israel*

Received March 7, 1997; revised June 12, 1997

**High resolution, dynamic GdDTPA-enhanced images of MCF7 human breast tumors in immunodeficient mice were analyzed at pixel resolution. The analysis, based on a physiological model, was performed by applying a nonlinear least-square algorithm using a color coded scale. The final output mapped at pixel resolution capillary permeability times surface area and fraction of extracellular volume, for each tumor slice. In addition, the output included assessment of the fit to the model by determining the proportion of variability ($R^2$) for each pixel. The spatial variation in the $R^2$ values served to identify regions where the predominant mechanism of enhancement was leakage from the intravascular volume to the extracellular volume ($R^2$ close to 1). In regions with low $R^2$ other mechanisms of enhancement appear to be dominating presumably diffusion within the extracellular space. As expected, in necrotic regions lacking microcapillaries and identified by analyzing $T_2$-weighted images of the same tumors, the model failed to fit the dynamic contrast enhanced data. The heterogeneous distribution of the determined pathophysiological features demonstrates the importance of recording and analyzing breast tumor images at high spatial resolution.** 

## INTRODUCTION

MRI techniques were investigated in the past in order to improve the detection and diagnosis of breast diseases (*1, 2* and references cited therein). Unfortunately, attempts to diagnose breast lesions by MRI on the basis of $T_1$ or $T_2$ contrast have been shown to be complex and indeterminate (*2, 3*). Alternatively, contrast-enhanced MRI has enabled the accurate delineation of breast cancer lesions (*1, 2* and references cited therein). Furthermore, dynamic contrast enhancement measurements demonstrated that the rate of change in signal enhancement is an important criterion for differentiation of breast masses (*4*).

Several approaches were applied to analyze the dynamic behavior following administration of a contrast agent. Initially modeling of tracer kinetics was developed and applied with modalities other then MRI, primarily to measure blood–brain barrier permeability (*5–9*). Extended modeling approaches have been developed for dynamic contrast-enhanced MRI (*10–12*), assuming a reversible exchange between the intravascular and the extracellular volume in the lesion and the rest of the body and clearance via the kidneys. These models attempted to provide physiological–pharmacokinetic and quantitative approaches to contrast-enhanced data (*10–17*), including breast carcinoma (*17–19*). Empirical approaches of image analysis based on kinetic analysis were also applied and were correlated with histological findings (*20, 21*). In most of the contrast-enhanced studies the recording parameters have been optimized to increase temporal resolution, but at the expense of spatial resolution (*20–23*). In the image analysis of such data the spatial resolution was further reduced by averaging signal intensity over selected regions of interest or over the whole tumor (*20–23*). It is clear, however, that most tumors are very heterogeneous and vary over space in terms of microscopic histopathological features (e.g., origin: tumor cells, fibrous cells, endothelial cells) and macroscopic histological features (such as cellularity—fraction of volume occupied by cells and presence and volume fraction of microvessels) as well as physiological features (such as blood flow rates in vessels, diffusion of nutrients and of tracers into and out of vessels and their diffusion in extravascular environments). Thus, as a result of tumor heterogeneity in microscopic and macroscopic terms the time evolution of contrast enhancement varies in space in an unpredictable manner, and therefore maintaining high spatial resolution in both the recording and analysis steps is very important.

Here we present a method for analyzing dynamic contrast-enhanced images at high spatial resolution, based on the derivation of Tofts and Kermode for analyzing contrast-enhanced MR images (*11*). This model was employed recently to analyze breast tumors in patients at low spatial resolution (*19*) and MCF7 human breast tumors implanted in nude mice at high spatial resolution (*24, 25*). We have extended this derivation to analyze at high spatial resolution a large number of MCF7 tumors, adding a statistical assessment of the capacity of this modeling approach to quantitatively characterize contrast agent kinetics. A computer program for image analysis at pixel resolution, based on this physiologi-

[1] To whom correspondence should be addressed.



1090-7807/97 $25.00

cal model, yielded maps of vascular surface area times permeability to GdDTPA (termed vascular permeability or permeability factor) and of fraction of volume accessible to the contrast agent, from which the fraction of extracellular volume as well as the fraction occupied by cells (cellularity) can be calculated. Assessment of the fit of the data to the model was obtained by calculating for each pixel the proportion of variability ($R^2$) to the equation derived from the model and then constructing an $R^2$ map. These maps enabled us to evaluate the model and the contribution of mechanisms neglected by the model (e.g., GdDTPA diffusion in the extracellular environment) to the dynamics of contrast enhancement. The results demonstrated the necessity to maintain high spatial resolution in both the recording and the analysis of the dynamic data. The detailed spatial distribution of cellularity and microvascular density and function may offer better specificity of diagnosis and improved ability to assess prognosis and response to therapy.

## EXPERIMENTAL

*Tumors.* MCF7 human breast cancer cells were inoculated into the flank of CDI-NU immunodeficient female mice as previously described (*26*). Prior to injection of cells a pellet of 17$\beta$ estradiol (0.72 mg/pellet, 60 days release time; Innovative Research, Sarasota, FL) was implanted underneath the back skin. A pellet of tamoxifen (5 mg/pellet, 45 days release time; Innovative Research, Sarasota, FL) was implanted in mice bearing tumors after the estrogen pellet was removed. All mice were anesthetized prior to the MRI measurements by an intraperitoneal injection of sodium pentobarbital at a dose of 0.06 mg/g wt.

*GdDTPA in the plasma.* N-Methylglucamine-GdDTPA [$(NMG)_2$GdDTPA] (Schering, Berlin, Germany) was injected as a bolus into the tail vein 20 min after administration of anesthesia, at a dose of 0.4 mmol/kg wt. At various time points after GdDTPA injection, a blood sample of $\sim$0.5 ml was drawn from each mouse (total number of mice = total number of blood samples = 20) and collected in a tube containing 100 $\mu$l heparin (Elkins-Sinn, Inc., New Jersey). Following centrifugation at room temperature for 10 min. (10,000$g$) supernatant plasma samples were separated and stored at $-20$°C, until analyzed by MRS.

*In vivo $^1H$ imaging.* MR images were recorded with a 4.7 T, Biospec spectrometer (Bruker) equipped with a $^1$H radiofrequency coil 7.5 cm in diameter. The protocol of each experiment included a multislice spin echo (SE) $T_2$-weighted imaging sequence with an echo time (TE) and a repetition time (TR) of 68 and 2400 ms, respectively, accumulating four averages. Subsequently, a precontrast $T_1$-weighted, SE image with TE of 15 ms and TR of 250 or 400 ms, of a selected slice from the center of the tumor was recorded with a time resolution of 1 or 1.5 min, respectively, accumulating two averages. This was followed by a bolus injection of 0.4 mmol/kg wt. of $(NMG)_2$GdDTPA into the tail vein of the mouse and a series of post-contrast images of the same central slice with the same $T_1$-weighted sequence. All images were recorded at the same spatial resolution with a slice thickness of 1 mm and an in-plane resolution of 195 $\times$ 390 $\mu$m. The overall experimental time lasted for about one hour.

$T_1$ relaxation time of MCF7 tumor tissue was measured *in vivo* by applying a SE imaging sequence with a constant TE of 15 ms and variable TR values (12 values) ranging from 400 to 5000 ms. In this experiment, images were recorded with a slice thickness of 1.5 mm and an in-plane resolution of 195 $\times$ 390 $\mu$m, accumulating two averages. The intensity of the MRI signal ($I_{SE}$) was analyzed according to

$$\begin{aligned} I_{SE} &= \mathrm{PD}*\exp(-\mathrm{TE}/T_2)*(1-\exp(-\mathrm{TR}/T_1)) \\ &= \mathrm{Constant}*(1-\exp(-\mathrm{TR}/T_1)). \end{aligned} \quad [1]$$

where PD is proton density. Average signal intensities in defined regions of interest (ROI) in the tumor, of about 20 pixels each, were used for determining $T_1$. ROIs of viable and necrotic regions identified by correlation with $T_2$-weighted images (*27*, *28*) were analyzed separately. The intensity versus TR curves were fitted to Eq. [1] using a nonlinear least-square fit program.

*$T_1$ and $T_2$ of plasma solutions.* $T_1$ and $T_2$ relaxation times of water protons in plasma solutions containing GdDTPA, either externally added or following administration into the tail vein, were measured at 4.7 T at 37°C, using conventional inversion recovery and Carr–Purcell–Meiboom–Gill sequences, respectively. From the relaxation times of solutions with externally added GdDTPA we have calculated the coefficients $R_1$ and $R_2$, which define the increase in relaxation rate per unit concentration of GdDTPA ($C$) according to

$$R_1 = [1/T_1 - 1/T_{10}]/C \quad [2a]$$

$$R_2 = [1/T_2 - 1/T_{20}]/C, \quad [2b]$$

where $1/T_{10}$ and $1/T_{20}$ are the corresponding relaxation rates of GdDTPA-free plasma solutions.

*The model and image analysis.* Analysis of GdDTPA-enhanced images was based on the kinetic model for MRI contrast enhancement derived by Tofts and Kermode (*11*). We summarize here the equations used by us in the image analysis programs. A more detailed description of the model and derived equations can be found in Ref. (*11*) and in a recent review by Tofts (*29*).

The concentration of the contrast agent in the plasma, $C_p(t)$, following its rapid equilibration over the whole vasculature is given by

$$C_p(t) = D[a_1\exp(-m_1t) + a_2\exp(-m_2t)], \quad [3]$$

where $D$ is the tracer dose, $a_1$ and $m_1$ are the amplitude and decay rate of the passive diffusion of the contrast agent from the intravascular volume to the extracellular volume of the whole body, $a_2$ and $m_2$ are the equivalent parameters for exchange and clearance through the kidneys.

In a tumor there are blood vessels and microcapillaries from which the contrast agent can passively diffuse into the extracellular volume. Each tumor pixel may contain capillaries; however, the fraction of intravascular volume is usually small and the enhancement is predominantly determined by the amount of contrast agent diffusing into the extracellular volume. For a pixel of volume $V_t$, a fraction of extracellular volume of $v_1$ and a concentration of contrast agent in the extracellular volume of $C_1$, the amount of the contrast agent per pixel is given by $v_1V_tC_1$. Since the diffusion of the contrast agent across the blood vessels is usually slower than the flow in the vessels, the change in time of the amount of GdDTPA per pixel is determined by the surface area ($S$) and permeability to the contrast agent ($P$) of the vasculature, yielding the differential equation (*11*)

$$v_1V_t(dC_1/dt) = [PS][C_p(t) - C_1(t)]. \quad [4]$$

$PS/V_t(\text{min}^{-1})$ defines a transfer constant $K$, termed here in short vascular permeability. The mean concentration of contrast agent over the whole pixel volume $C_t(t) = v_1C_1(t)$ determines the extent of enhancement. Solving Eq. [4] and substituting Eq. [3] yields a three exponential curve for the modulation of the mean concentration of contrast agent with time

$$C_t(t) = D[b_1\exp(-m_1t) + b_2\exp(-m_2t) + b_3\exp(-Kt/v_1)], \quad [5]$$

where

$b_1 = Ka_1/(K/v_1 - m_1)$, $b_2 = Ka_2/(K/v_1 - m_2)$ and $b_3 = -(b_1 + b_2)$.

In order to analyze the enhancement data we initially measured the concentration of the contrast agent in blood samples drawn at various time points after its injection and determined the average values of $a_1$, $m_1$, $a_2$, and $m_2$ in immunodeficient mice by using Eq. [3]. The remaining two unknown parameters, $K$, the vascular permeability, and $v_1$, the fraction of extracellular volume, were then determined from the time evolution of signal enhancement $[I(t) - I(0)]/I(0)$ which depends on the modulation of the mean concentration of contrast agent $C_t(t)$ according to the following equation, derived for a SE sequence:

$$\text{Enhancement}(t) = \frac{\exp[-R_2C_t(t)\text{TE}]\{1 - 2\exp[-(\text{TR} - \text{TE}/2)(1/T^t_{10} + R_1C_t(t))] + \exp[-\text{TR}(1/T^t_{10} + R_1C_t(t))]\}}{\{1 - 2\exp[-(\text{TR} - \text{TE}/2)/T^t_{10}] + \exp(-\text{TR}/T^t_{10})\} - 1}, \quad [6]$$

where $T^t_{10}$ is the $T_1$ of the tumor before administration of GdDTPA. We have verified that under the applied experimental conditions (the dose of GdDTPA and the MRI spin echo parameters) the enhancement increased linearly with GdDTPA concentration in the range of 0–1.5 m*M*.

A computer program which included a nonlinear least-square algorithm (Levenberg–Marquardt method (*30*) was used to fit the enhancement-time curve in each pixel (Eq. [6]) of tumor tissue with the insertion of $C_t(t)$, according to Eq. [5]. Utilizing this program yielded the best fitted values of $K$ and $v_1$. An ROI of the entire tumor tissue was defined in a $T_2$-weighted image and was then retained in all the contrast-enhanced images of the same tumor. Assessment of the quality of the fitting for each pixel was obtained by calculating the proportion of variability $R^2$ defined by

$$R^2 = 1 - \frac{\Sigma\,[\text{Enhancement}(t) - \text{fitted enhancement value}(t)]^2}{\Sigma\,[\text{Enhancement}(t) - \text{averaged enhancement value}]^2}. \quad [7]$$

In performing this analysis we observed that the program failed to fit the enhancement curves of certain pixels to the model-based equation. It is clear that in necrotic regions that lack the presence of capillaries the enhancement could not be fitted to the model. Also in pixels where the vascular permeability was very low and the enhancement was dominated by diffusion through the extracellular volume from nearby pixels the fitting was relatively poor. Thus the $R^2$ map also provided assessment of the distribution of pixels which were devoid of capillaries and of pixels which appeared to have capillaries with very low permeability.

## RESULTS

*Determination of $T_1$ in tumors.* $T_1$ values, of MCF7 tumor tissue in the absence of GdDTPA ($T_{10}$), were determined in viable cancer tissues and in necrotic areas, and were found to be 2.4 ± 0.1 s ($n$ = 3) and 3.0 ± 0.4 s ($n$ = 3), respectively, with $T_1$ more homogeneous in viable regions. However, in the $T_1$-weighted images recorded prior to GdDTPA administration, the contrast between necrotic and viable regions was too low for their resolution (see example in Fig. 1). An average $T_1$ value was therefore applied in the image analysis of contrast enhancement (Table 1). As demonstrated previously (*26, 27*), necrotic and viable regions could be easily resolved in the $T_2$-weighted images (Fig. 1).

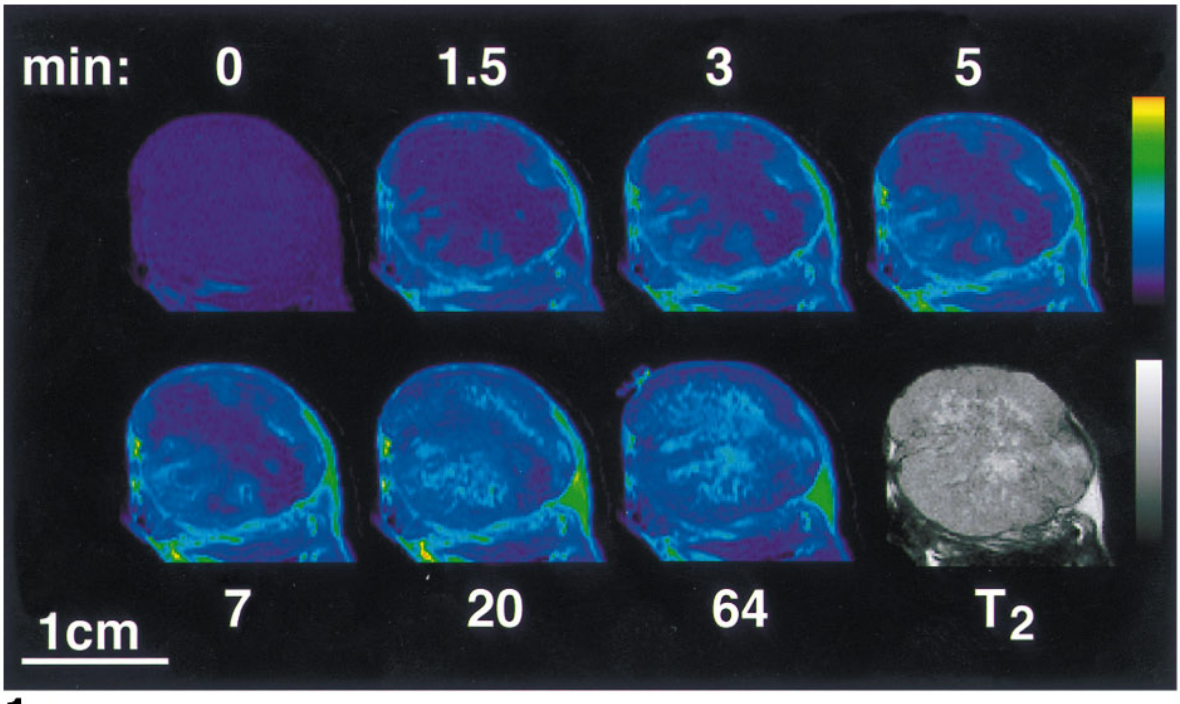
min: 0
1.5
3
5
7
20
64
T2
1cm

1

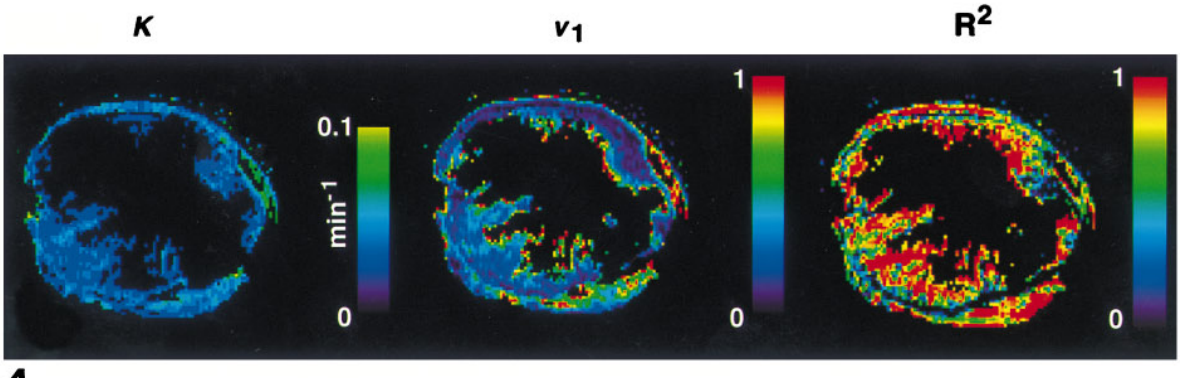
K
v1
R2
0.1
min-1
0
1
0
1
0

4

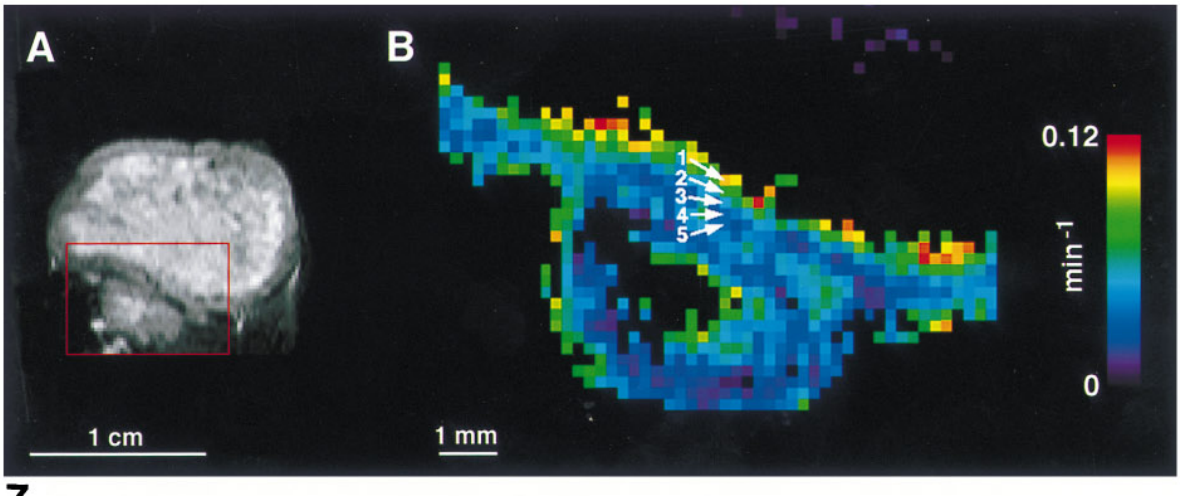
A
B
1 cm
1 mm
1
2
3
4
5
0.12
min-1
0

7

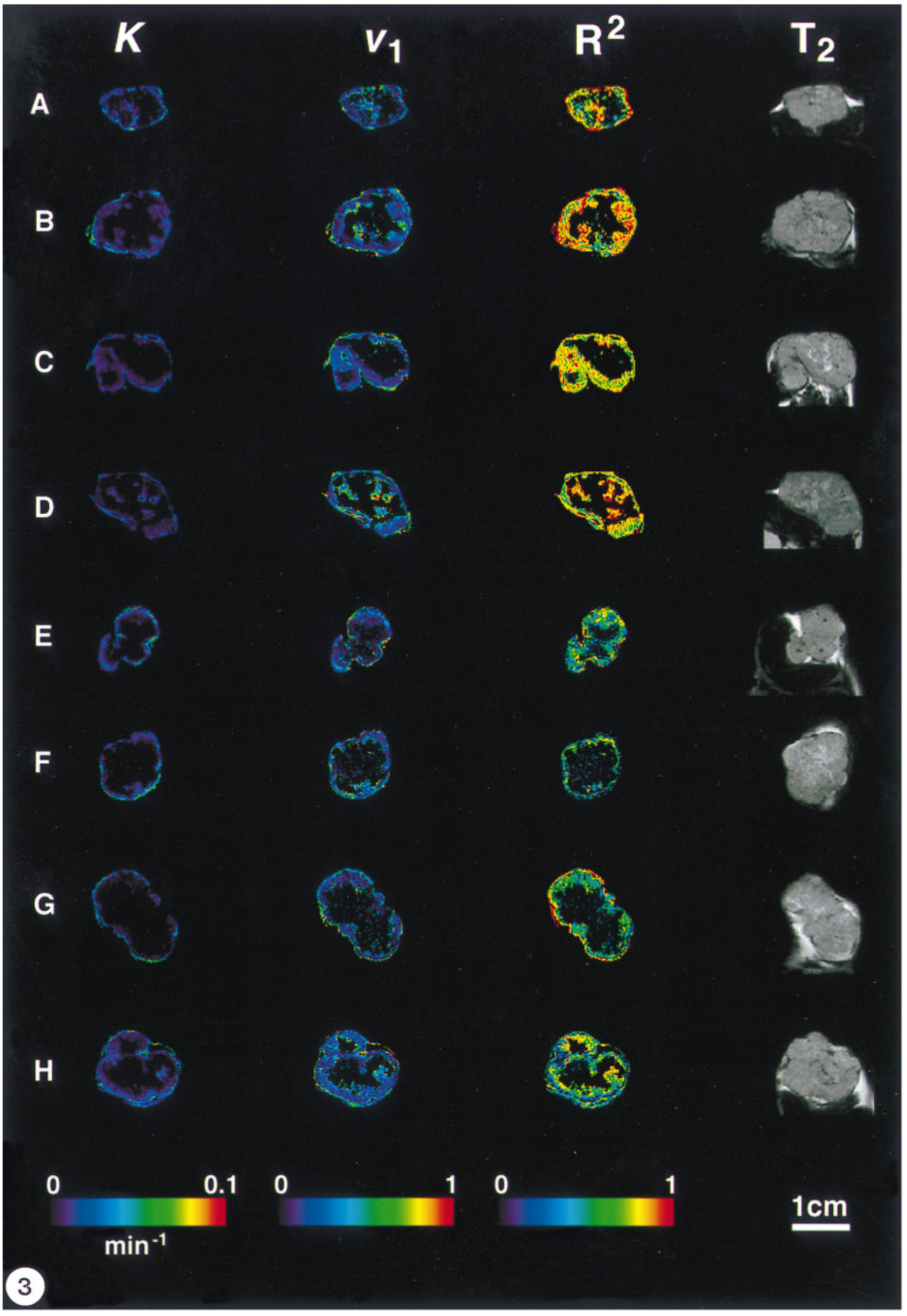
K
$v_1$
$R^2$
$T_2$
A
B
C
D
E
F
G
H
0
0.1
min$^{-1}$
0
1
0
1
1cm
3

**TABLE 1**
**Parameters Used in the Image Analysis**

| Parameter | Value[a] |
|---|---|
| Tumor $T_1$ ($T^t_{10}$) | 2.7 sec[b] |
| $T_1$ of plasma ($T_{10}$) | 2.40 ± 0.06 sec (n = 3)[c] |
| $T_2$ of plasma ($T_{20}$) | 363 ± 35 msec (n = 3)[c] |
| Relaxivity rates of plasma | |
| $R_1$ | 4.3 $sec^{-1}$ $mM^{-1}$, r = 0.999 |
| $R_2$ | 4.9 $sec^{-1}$ $mM^{-1}$, r = 0.999 |
| Plasma curve amplitudes | |
| $a_1$ | 4.3 kg/liter |
| $a_2$ | 3.2 kg/liter |
| Plasma curve decay rates | |
| $m_1$ | 0.430 $min^{-1}$ |
| $m_2$ | 0.057 $min^{-1}$, r = 0.976[d] |

[a] Values were determined as described under Experimental.
[b] Obtained by averaging $T_1$ of viable and necrotic ROIs.
[c] Mean ± standard deviation.
[d] Correlation coefficient for fitting $a_1$, $a_2$, $m_1$, and $m_2$.

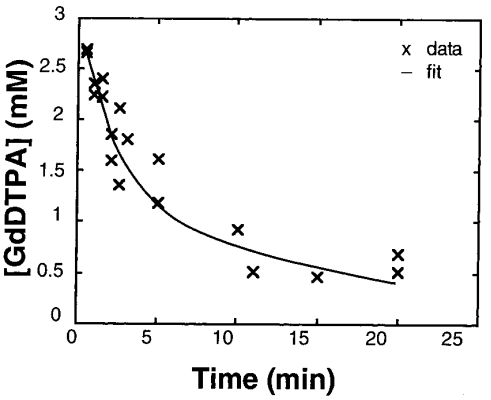


**FIG. 2.** Modulation of GdDTPA in the plasma of mice. Concentrations were determined following a bolus injection of 0.4 mmol/kg GdDTPA to CDI-NU immunodeficient female mice as described under Experimental. The line is a biexponential curve fitted to Eq. [3] (correlation coefficient $r = 0.976$). The values of the best fitted parameters $a_1$, $a_2$, $m_1$, $m_2$ are given in Table 1.

*$T_1$ and $T_2$ in plasma samples.* $T_1$ and $T_2$ relaxation times of water protons in plasma solutions containing increasing concentrations of externally added GdDTPA were measured at 37°C, as described under Experimental. The measured $T_1$ and $T_2$ of water protons in GdDTPA-free solutions ($T_{10}$ and $T_{20}$) as well as the values of the coefficients $R_1$ and $R_2$ defining the increase in the relaxation rates per unit concentration of GdDTPA are summarized in Table 1.

*GdDTPA pharmacokinetics in nude mice.* The pharmacokinetics of GdDTPA after i.v. injection was determined by measuring the water $T_1$ of blood samples drawn from the mice. The $T_1$ relaxation times were then related to GdDTPA concentration using Eq. [2a] and the determined $R_1$ value (Table 1). Figure 2 demonstrates the experimental results and the curve derived by fitting the data to a biexponential decay equation (Eq. [3]). The best fitted amplitudes ($a_1$ and $a_2$) and decay rates ($m_1$ and $m_2$), characteristic for GdDTPA pharmacokinetics in nude mice, are summarized in Table 1.

*Analysis of dynamic GdDTPA enhanced MRI of MCF7 tumors.* The pattern of contrast distribution with time indicated the presence of different pathways of regional contrast enhancement: (1) Fast contrast enhancement at the capsule surrounding the tumors and in few intratumoral loci, (2) moderate to slow contrast enhancement in most intratumoral viable regions where maximum contrast enhancement was reached within 5–20 min, and (3) delayed slow enhancement in intratumoral necrotic regions where contrast enhancement was still rising after 40 min. (Fig. 1). Image analysis at pixel resolution of the dynamic evolution of GdDTPA, according to the model described above, yielded maps of capillary permeability times surface area ($K$), termed permeability factor and of extracellular fraction accessible to the contrast agent ($v_1$). Figure 3 demonstrates constructed images of permeability factor and of fraction of extracellular volume of central tumor slices in eight control mice and their corresponding $R^2$ images. $T_2$-weighted images of the same slices are also shown for demonstrating the distribution of gross histopathological features, primarily localization of necrosis. As was demonstrated by us earlier (*26, 27*), control tumors growing in the presence of estrogen to about 1 $cm^3$ size were mostly composed of viable cancer

**FIG. 1.** Images of MCF7 tumor recorded in a dynamic contrast-enhanced study. Control tumor grown in the presence of estrogen. Images of a central slice, recorded with a spin echo sequence (TE/TR = 15/400 ms) as described under Experimental. A $T_2$-weighted image of the same tumor slice is presented at the lower right side.

**FIG. 3.** Analysis of contrast-enhanced images of control MCF7 tumors treated with estrogen. Maps of permeability factor ($K$), fraction of free extracellular volume ($v_1$), and $R^2$ of a central slice in eight MCF7 tumors grown in the presence of estrogen. A $T_2$-weighted image of the same slice is demonstrated on the right. The maps were derived from analysis of GdDTPA-enhanced images recorded with a spin echo sequence with TE of 15 ms and TR of 400 ms (tumors A–D) or 250 ms (tumors E–H).

**FIG. 4.** Analysis of contrast-enhanced images of a control MCF7 tumor. Maps of permeability factor ($K$), fraction of free extracellular volume ($v_1$), and $R^2$ of a central slice of the MCF7 tumor shown in Fig. 1.

**FIG. 7.** Demonstration of the importance of high spatial resolution. (A) $T_2$-weighted image of MCF7 tumor treated with tamoxifen (tumor H in Fig. 6) the marked region is demonstrated in (B). (B) A permeability factor map of the area defined in (A). Five pixels are marked with arrows in the permeability factor ($K$) map. The fitted $K$, $v_1$, and $R^2$ values for these pixels and for the ROI of these five pixels are summarized in Table 2. Note that high permeability factor values are observed in pixels at the boundary of necrosis (necrosis appears bright in the $T_2$-weighted image).

cells (gray in the corresponding $T_2$-weighted images) with few scattered necrotic loci (characterized by a higher signal intensity in the $T_2$-weighted images) mainly at the center of the tumors. The stromal capsule around the tumors is also clearly discerned by its low intensity in the $T_2$-weighted images. The image analysis-derived maps showed regions of high vascular permeability and high fraction of extracellular volume at the stromal capsule surrounding the tumor. In most of these regions the fit was good with $R^2$ values in the range 0.7–1.0.

A better fit, demonstrated by higher $R^2$ values, was obtained in the analysis of images that were recorded with the longer TR of 400 ms than that obtained with TR of 250 ms (Fig. 3). This is primarily attributed to the better signal-to-noise ratio in the former images.

Figure 4 demonstrates maps of permeability factor and fraction of extracellular space as well as the corresponding $R^2$ map derived from analysis of the contrast-enhanced images of the tumor demonstrated in Fig. 1. In pixels that were best fitted to the model ($R^2$ in the range 0.7–1), the predominant mechanism of contrast enhancement was diffusion from the intravascular space to the extracellular volume via permeable capillaries. Typical values in peripheral pixels that exhibited a very fast initial rate followed by a fast decay were: $K$ in the range of 0.05–0.12 $\text{min}^{-1}$ and $v_1$ in the range of 0.8–1. In intratumoral viable regions typical fitted $K$ values ranged between 0.005 and 0.06 $\text{min}^{-1}$ and $v_1$ values ranged between 0.2 and 0.7. As expected, contrast enhancement curves in pixels showing necrosis could not be fitted to the model based equation (Eq. [6]) and were marked black in the maps derived by image analysis (Figs. 3–5). In these regions the enhancement was clearly dominated by diffusion through the extracellular volume from pixels in the vicinity that contained permeable capillaries. Pixels with moderate to low fitting ($R^2 < 0.7$) appeared predominantly in viable tumor regions. In these viable regions there must be capillaries through which nutrients are distributed. However, the permeability of these capillaries to the contrast agent might be low as is the case in capillaries of normal tissue. It appears that in these regions both slow diffusion from the intravascular volume to the extracellular volume and diffusion through the extracellular volume from the surrounding pixels contribute to the enhancement curves. Fitted signal enhancement curves for typical tumor pixels are shown in Fig. 5. In regions with high permeability factor the initial rate of enhancement was also high as expected when enhancement is linearly increasing with the concentration of the contrast agent (as is the case in our studies). In regions where the fraction of extracellular space was relatively low (high cellularity) the maximum of contrast enhancement was also low, as expected from the model applied here. An example of a curve which could not be fitted is also shown (Fig. 5, curve 4). The $T_2$-weighted image clearly demonstrates that in this pixel the intensity is indicative of necrosis. Enhancement did occur in this pixel but it was delayed, presumably since it was dominated by diffusion from other areas through the free extracellular space. This later-in-time and slower process is not accounted for by the model.

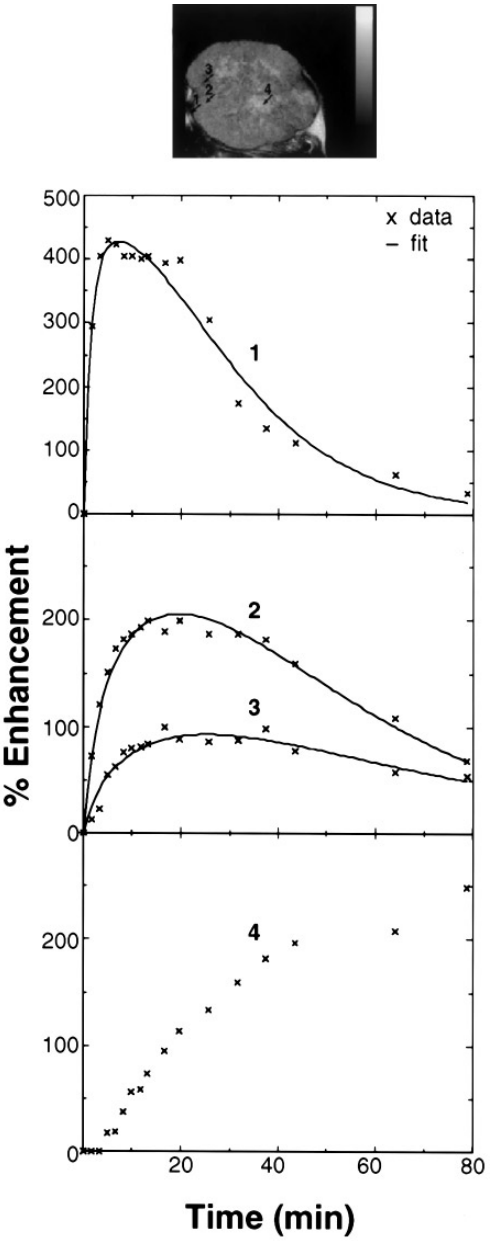


**FIG. 5.** Analysis of enhancement curves in selected pixels. Images were recorded with a SE sequence with TE/TR = 15 ms/400 ms. The lines are best fitted curves to Eq. [6]. (1) An enhancement curve for a typical tumor pixel from a peripheral region: $K = 0.117\ \text{min}^{-1}$, $v_1 = 0.78$, $R^2 = 0.96$. (2) An enhancement curve for an intratumoral pixel with fast enhancement: $K = 0.019\ \text{min}^{-1}$, $v_1 = 0.56$, $R^2 = 0.98$. (3) An enhancement curve for an intratumoral pixel with slow enhancement: $K = 0.006\ \text{min}^{-1}$, $v_1 = 0.31$, $R^2 = 0.93$. (4) An enhancement for a slowly enhancing pixel in a necrotic region. This data could not be fitted to Eq. 6. The pixels are marked with arrows in a corresponding $T_2$-weighted image.

Figure 6 demonstrates constructed images of permeability factor and of fraction of extracellular volume and the corresponding $R^2$ images of central tumor slices in eight mice treated

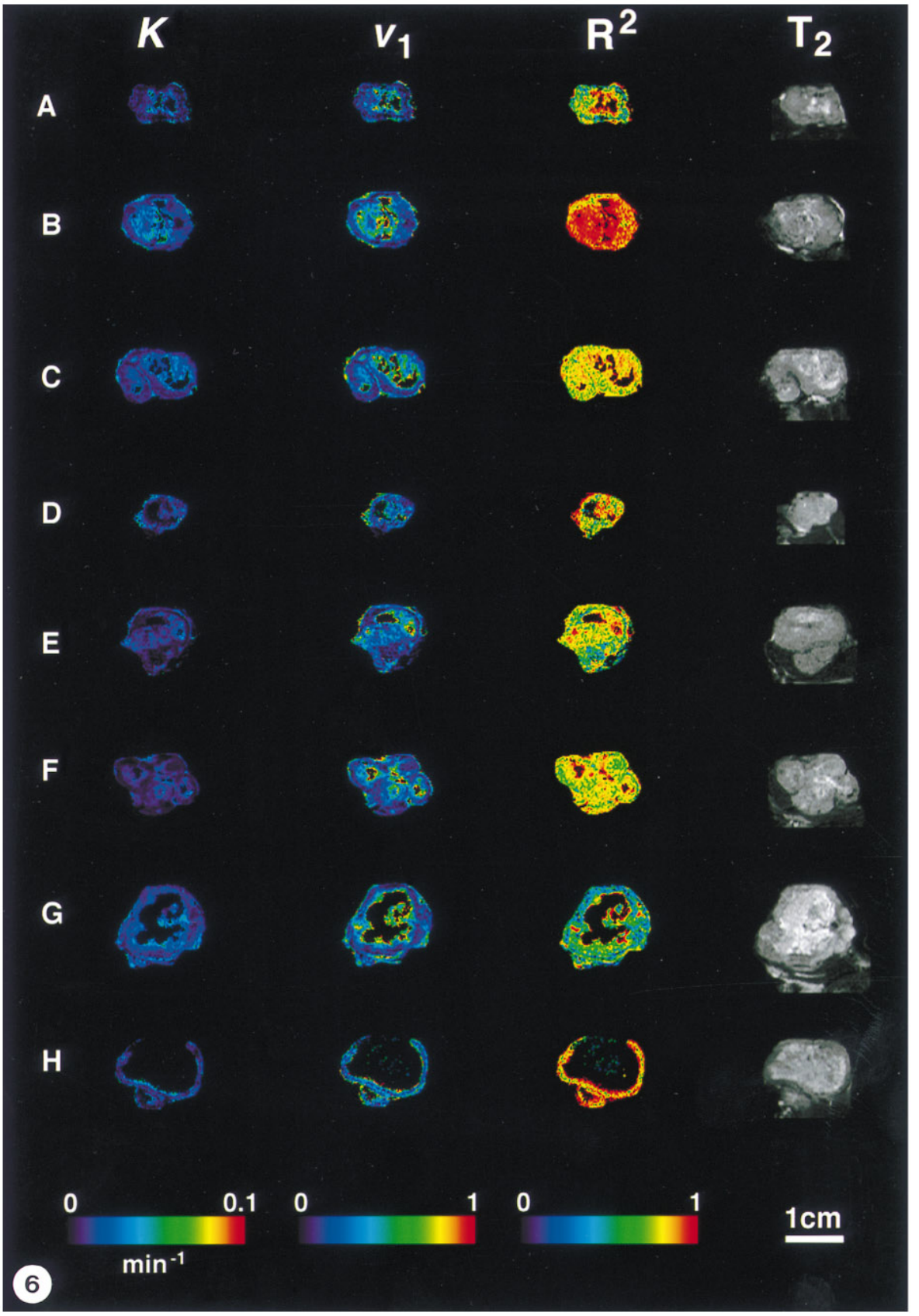
K
$v_1$
$R^2$
$T_2$
A
B
C
D
E
F
G
H
0
0.1
min$^{-1}$
0
1
0
1
1cm
6

**TABLE 2**
**$K$, $v_1$, and $R^2$ Values in an Intratumoral Region**

| Pixel no. | $K$ (min$^{-1}$) | $v_1$ | $R^2$ |
|---|---|---|---|
| 1 | 0.049 | 0.86 | 0.98 |
| 2 | 0.035 | 0.61 | 0.97 |
| 3 | 0.018 | 0.39 | 0.88 |
| 4 | 0.011 | 0.22 | 0.71 |
| 5 | 0.011 | 0.18 | 0.75 |
| ROI: 1–5 | $K_{ROI} = 0.020$ | $v_{1ROI} = 0.51$ | $R^2_{ROI} = 0.88$ |

*Note.* Analysis of 5 adjacent pixels marked with arrows in Fig. 7B. $K_{ROI}$, $v_{1ROI}$ *and* $R^2_{ROI}$ *values were obtained by analyzing the enhancement curve of the ROI of these 5 pixels.*

with the antiestrogenic drug tamoxifen. $T_2$-weighted images of the same slices show the localization of necrosis. As was previously described by us, massive central necrosis is observed as a result of tamoxifen therapy (*26–28, 31*). In the tamoxifen treated tumors (Fig. 6), as in the estrogen-treated tumors (Figs. 3 and 4), pixels with higher values of permeability factor, $K$, and fraction of extracellular space, $v_1$, were located in peripheral areas. Uniquely, in intratumoral regions at the boundaries of necrosis the permeability factor and the fraction of extracellular volume were augmented with $K$ in the range of 0.03–0.07 min$^{-1}$ and $v_1$ in the range of 0.6–1. In the remaining viable tumor areas, $K$ and $v_1$ were of low to moderate values, as in viable regions of estrogen-treated tumors. As expected the model failed to fit the enhancement curves in necrotic regions devoid of capillaries (pixels coded black).

In regions where a good fit of the enhancement curves to the model was obtained it was possible to resolve tumor heterogeneity in terms of the vascular permeability and extracellular volume. Fitted $K$ and $v_1$ values for five adjacent pixels in a tamoxifen-treated tumor (shown in Fig. 7) and their separate $K$ and $v_1$ values, as well as fitted $K$ and $v_1$ values that were obtained by analyzing all five pixels as one ROI, are summarized in Table 2. The analysis at pixel resolution demonstrates that although these pixels are adjacent, they are characterized by different permeability factors and fractions of extracellular space: In the vicinity of necrosis (pixel 1 and pixel 2) $K$ and $v_1$ are high, and both values decrease with increased distance from necrosis into the viable tissue (pixels 3 to 5). On the other hand the average values of the permeability factor and of the fraction of extracellular space (see Table 2) obtained by analysis at a lower spatial resolution (ROI of 5 pixels) do not reveal this unique change in the vicinity of necrosis. Similar variations in these two parameters have been found in all the other tumors (see maps in Fig. 6). Thus, this typical example demonstrates the importance of maintaining high spatial resolution in both the recording and analysis steps.

## DISCUSSION

The time-dependent distribution of a contrast agent injected into the vascular system can be divided to several steps. After a bolus injection, there is initially a fast equilibration step in the intravascular volume. This step is followed by a reversible diffusion of the contrast agent through the capillaries' wall from the intravascular to the extravascular space. For a contrast agent that cannot enter into cells, such as GdDTPA, the diffusion from the intravascular to the extracellular space is followed by diffusion in the extravascular–extracellular environment. In parallel to this step the contrast agent is being gradually cleared out from the vascular system. For example, GdDTPA is cleared out via the kidneys into the urine. The intracapillary volume in a tumor tissue is relatively small, less than 10% of a unit volume (*32*), and therefore the contribution from this volume to the enhancement is small. Due to the higher permeability of tumor capillaries the diffusion of a contrast agent from the intravascular to the extracellular volume is relatively fast. In addition, the unique patterns of tumor growth lead to the presence of regions with large fractions of extracellular space and therefore to increased amounts of contrast agent in these regions. The augmented contrast enhancement in tumors is associated with these two unique physiological/histological features of tumors.

The time resolution and overall experimental time used in the study presented here was adapted to monitor predominantly the reversible diffusion between the intravascular and the extracellular volumes as well as within the extracellular volume. In order to resolve tumor heterogeneity we have used the maximum possible spatial resolution under our experimental conditions. The image analysis was based on the model developed by Tofts and Kermode (*11*) which focuses on the reversible diffusion between the intravascular and extracellular spaces, neglects the contribution from the intravascular volume, and does not take into account diffusion within the extracellular space. This model was previously adjusted by us to study angiogenic processes in MCF7 tumors following tamoxifen therapy (*24, 25*). In this work, by including assessment at pixel resolution of the fitting of the model-based equation to the enhancement curves, we were able to resolve variations within the tumor and to demonstrate the advantages and limitations of this model.

As explained above, the equations were derived assuming

**FIG. 6.** Analysis of contrast enhanced images of MCF7 tumors treated with tamoxifen. Maps of permeability factor ($K$), fraction of free extracellular volume ($v_1$), and $R^2$ of a central slice derived from analysis of GdDTPA-enhanced images. A $T_2$-weighted image of the same slice is shown on the right, demonstrating high fraction of necrosis as a result of tamoxifen treatment (*25, 29*). Images were recorded with a spin echo sequence with TE of 15 ms and TR of 400 ms (tumors A–C, E–H) or 250 ms (tumor D).

that signal enhancement is dominated by the reversible diffusion between the intravascular and the extracellular spaces and is therefore due to the presence of permeable capillaries in each pixel. Thus the model was not adequate for describing the time evolution of contrast enhancement in pixels devoid of capillaries, such as necrotic regions that nevertheless were enhanced. In the necrotic regions signal enhancement was presumably dominated by diffusion through the extracellular volume from nearby pixels. In other regions in the tumor the fitting varied from very good to very poor. Correlation with histology and with $T_2$-weighted images indicated poor fitting in parts of viable tumor tissue. The presence of blood capillaries in these regions is evident from the viability of the tissue and from the presence of endothelial cells (*26*). Thus, in addition to permeation of contrast agent from capillaries within these pixels according to the model it appears that diffusion through the extracellular volume from nearby pixels, which is not included in the model, contributed to the contrast enhancement curves. Although the model could not fit with the same accuracy the enhancement curves of all tumor pixels, the $R^2$ maps helped identify regions where the mechanism of contrast enhancement was predominantly by permeation from the microvascular volume into the extracellular volume and regions where presumably diffusion through the extracellular volume dominated the enhancement curves. In the former regions tumor heterogeneity in terms of permeability factor and fraction of extracellular space could be quantitatively mapped.

Dynamic studies of contrast enhancement in breast tumors demonstrated that the rate of change in signal intensity is an important parameter for the distinction of breast masses (*4*). This led to further studies with an emphasis on temporal resolution (at the expense of spatial resolution) and on the first steps of equilibration in the intravascular space and early diffusion into the extracellular space of the tissue. In clinical studies the enhancement in breast lesions reached its maximum 1.5–6 min after injection of a bolus of GdDTPA. Hoffman *et al.* (*18*) have found that the enhancement curve reached its maximum within 90 s, and thus high temporal resolution of about 18 s was applied. In our study we have optimized the spatial resolution, extending the time scale to include reverse diffusion from the extracellular space to the intravascular volume. Maximum contrast enhancement was reached within 12–20 min in viable tumor regions, while enhancement of inner necrotic regions was still rising after 40 min. The slow kinetics of contrast enhancement in these tumors enabled us to acquire images with a temporal resolution of 1.5 min and still have at least 4–5 sampling points before signal enhancement reached a maximum value.

From the dynamic uptake of GdDTPA in breast tumors of patients Tofts *et al.* (*19*) estimated average values for the whole tumor slice of $K$ in the range of 0.1–1.2 $min^{-1}$, and for $v_1$ in the range of 0.3–0.8. Hoffmann *et al.* (*18*) extracted a parameter that is equal to $K/v_1$. The fitting routine for a representative ROI of a single case of breast carcinoma estimated a ratio $K/v_1$ of 7.59 $\pm$ 1.9 $min^{-1}$, yielding, for the highest possible $v_1$ of 1, a lower limit for the permeability factor of about 7.59 $min^{-1}$. Thus, in human breast lesions the fast uptake appeared to be associated with a markedly higher permeability factor than in tumors implanted in mice, where the permeability factor ranged between 0 and 0.1 $min^{-1}$.

Augmented $K$ and $v_1$ values were observed in intratumoral regions located at the vicinity of necrosis (Fig. 6 and Fig. 7). We have previously shown that the high permeability factor in these intratumoral regions is associated with stress-induced angiogenesis and is augmented in tumors responding to tamoxifen therapy (*25*). Indeed, here too, the tamoxifen treated tumors show a high permeability factor in the vicinity of necrosis. Furthermore the induced angiogenesis appears to result from up-regulation of the expression of vascular endothelial growth factor (also known as vascular permeability factor VEGF/VPF) in cells that are adjacent to necrotic loci (*33–36*). This stress-induced angiogenesis appears to be the dominant mechanism of intratumoral contrast enhancement (*25*). Recent studies indicated that VEGF/VPF is likely to have an important role in the vascular and stromal changes necessary for growth, and possibly the metastatic spread of breast cancer, and may also be of a prognostic value (*37, 38*). At low spatial resolution, intratumoral pixels that exhibit high contrast enhancement due to the presence of dense and leaky capillaries in the vicinity of necrosis might be overlooked when the spatial resolution is low, as demonstrated in Fig. 7 and Table 2. It is therefore clear that a better and more accurate characterization of pathophysiological features in breast tumors or other lesions require imaging and analysis at high spatial resolution.

High extracellular space and high permeability were observed in part of the peripheral pixels that exhibited a rapid initial contrast enhancement followed by a fast decay. These peripheral pixels could have high density of capillaries or even a vessel of a pixel dimension. In our model, the volume of the capillaries was neglected, and we could not therefore differentiate between enhancement due to very high vascular volume (on the order of a pixel volume) and that due to high fraction of extracellular space. In order to characterize breast tumors as fully as possible the blood volume or vascularity should be determined separately. This may be achieved *in vivo* by using contrast agents with a very low permeability through the vessels. Visual inspection of the tumors before sectioning for histology confirmed the presence of relatively large vessels around the tumor margin. In addition, histological examinations indicated the presence of capillaries at high density, in the stromal capsule surrounding the tumor.

One of the assumptions in the model we have used is that the flow of contrast agent from the blood into the extracellular space is slower than the blood flow (*11*). If blood flow would have been rate limiting, then changes in enhancement would have paralleled the change in GdDTPA concentration in the blood circulation. The decay of GdDTPA in the blood of the mice (Fig. 2) was fast and was characterized by

decay constants ($1/m_1$ and $1/m_2$) of 2.3 min for the plasma–extracellular space exchange and 17.5 min for the plasma–kidneys exchange, compared to 6.9 and 90 min, respectively in humans (*39*). Inspection of signal enhancement curves (Fig. 5) showed that in most of the intratumoral pixels the increase in signal intensity proceeded predominantly when the concentration of GdDTPA in the blood reached 20–30% of its maximum value. Thus, signal enhancement occurred in a ''time window'' where the concentration of the contrast agent in the blood circulation reached an apparent steady state, and therefore the contribution from flowing blood remained constant. In clinical studies, since the decay of GdDTPA in the plasma is slower and the permeability factor can reach high values, the derived permeability factor may contain a flow component (*19*).

In summary, accurate $K$ and $v_1$ values were determined in regions where the predominant mechanism of contrast enhancement was reversible diffusion from the intravascular to the extracellular environments. Assessment of the model ($R^2$) enabled us to characterize patterns of contrast enhancement and to evaluate the contribution of the permeability of the microvessels (to GdDTPA) and the diffusion of GdDTPA in the extracellular environment. Furthermore, we have demonstrated the importance of imaging and analysis at high spatial resolution in order to reveal the heterogeneous nature of tumor morphology and vasculature. A similar approach in breast MRI of patients may improve the specificity of diagnosis and provide assessment of prognosis.

## ACKNOWLEDGMENTS

We thank Dr. Peter Bendel and Raanan Margalit for their assistance in the course of this work. This work was supported by the National Cancer Institute Grant CA 42238.

## REFERENCES

1. S. E. Harms and D. P. Flaming, *J. Magn. Reson. Imaging* **3,** 277 (1993).
2. S. H. Heywang-Kobrunner, *Invest. Radiol.* **29,** 94 (1994).
3. N. Dash, A. R. Lupetin, R. H. Daffner, Z. L. Deeb, R. J. Sefczek, and R. L. Schapiro, *Am. J. Roentgenol.* **146,** 119 (1986).
4. W. A. Kaiser and E. Zeitler, *Radiology* **170,** 681 (1989).
5. C. S. Patlak, R. G. Blasberg, and J. D. Fenstermacher, *J. Cereb. Blood Flow Metab.* **3,** 1 (1983).
6. R. A. Hawkins, M. E. Phelps, S. C. Huang, J. A. Wapensik, P. D. Grimm, R. G. Parker, G. Juillard, and P. Greenberg, *J. Cereb. Blood Flow Metab.* **4,** 507 (1984).
7. F. Iannotti, D. Fieschi, B. Alfano, P. Picozzi, L. Mansi, C. Pozzilli, A. Panzo, G. D. Veecchio, G. L. Lanzi, M. Salvatore, and P. Conforti, *J. Comput. Assist. Tomogr.* **11,** 390 (1987).
8. V. Dhawan, A. Poltorak, J. R. Moeller, J. O. Jarden, S. C. Stother, H. Thaler, and D. A. Rotenberg, *Phys. Med. Biol.* **34,** 1773 (1989).
9. W. T. I. Yeung, T.-Y. Lee, R. F. D. Maestro, R. Kozak, and T. Brown, *J. Neuro. Oncol.* **14,** 177 (1992).
10. H. B. W. Larsson, M. Stubgaard, J. L. Frederiksen, M. Jensen, O. Henriksen, and O. B. Paulson, *Magn. Reson. Med.* **16,** 117 (1990).
11. P. S. Tofts and A. G. Kermode, *Magn. Reson. Med.* **17,** 357 (1991).
12. G. Brix, W. Semmler, R. Port, L. R. Schad, G. Layer, and W. J. Lorenz, *J. Comput. Assist. Tomogr.* **15**(4), 621 (1991).
13. J. Kenny, U. Schmiedl, K. Maravilla, F. Starr, M. Graham, A. Spence, and J. Nelson, *Magn. Reson. Med.* **27,** 68 (1992).
14. P. Gowland, P. Mansfield, P. Bullock, M. Stehling, B. Worthington, and J. Firth, *Magn. Reson. Med.* **26,** 241 (1992).
15. V. S. Vexler, O. Clement, H. Schmitt-Willich, and R. C. Brasch, *J. Magn. Reson. Imaging* **4,** 381 (1994).
16. M. Y. Su, J. C. Jao, and O. Nalcioglu, *Magn. Reson. Med.* **32,** 714 (1994).
17. K. M. Donahue, R. M. Weisskoff, D. J. Parmelee, R. J. Callahan, R. A. Wilkinson, J. B. Mandeville, and B. R. Rosen, *Magn. Reson. Med.* **34,** 423 (1995).
18. U. Hoffmann, G. Brix, M. V. Knopp, T. HeB, and W. J. Lorenz, *Magn. Reson. Med.* **33,** 506 (1995).
19. P. S. Tofts, B. Berkowitz, and M. D. Schnall, *Magn. Reson. Med.* **33,** 564 (1995).
20. A. M. Zagdanski, R. Sigal, J. Bosq, J. P. Bazin, D. Vanel and R. Di Paola, *Am. J. Neuroradiol.* **15,** 1359 (1994).
21. C. Frouge, J. M. Guinebretiere, G. Contesso, R. Di Paola, and M. Blery, *Invest. Radiol.* **29,** 1043 (1994).
22. S. D. Kennedy, L. S. Szczepaniak, S. L. Gibson, R. Hilf, T. H. Foster, and R. G. Bryant, *Magn. Reson. Med.* **31,** 292 (1994).
23. C. A. Hulka, B. L. Smith, D. C. Sgroi, L. Tan, W. B. Edmister, J. P. Semple, T. Campbell, D. B. Kopans, T. J. Brady, and R. M. Weisskoff, *Radiology* **197,** 33 (1995).
24. E. Furman-Haran, R. Margalit, D. Grobgeld, and H. Degani, Abstracts of the International Society for Magnetic Resonance in Medicine, Nice, France Vol. 3, p. 1597 (1995).
25. E. Furman-Haran, R. Margalit, D. Grobgeld, and H. Degani, *Proc. Natl. Acad. Sci. U.S.A.* **93,** 6247 (1996).
26. E. F. Haran, A. F. Maretzek, I. Goldberg, A. Horowitz, and H. Degani, *Cancer Res.* **54,** 5511 (1994).
27. E. Furman, R. Margalit, P. Bendel, A. Horowitz, and H. Degani, *Cancer Commun.* **3**(9), 287 (1991).
28. H. Degani, E. Furman, and S. Fields, *Clin. Chim. Acta,* **228,** 19 (1994).
29. P. S. Tofts, *J. Magn. Reson. Imaging* **7,** 91 (1997).
30. S. A. Teukolsky, W. T. Vetterling, and B. P. Flannery, ''Numerical Recipes in C,'' 2nd ed., p. 683, Cambridge Univ. Press, Cambridge, UK (1994).
31. E. Furman-Haran, R. Margalit, A. F. Maretzek, and H. Degani, *J. Magn. Reson. Imaging* **6,** 195 (1996).
32. R. K. Jain, *Sci. Am.* **271,** 58 (1994).
33. D. Shweiki, A. Itin, D. Soffer, and E. Keshet, *Nature* **359,** 843 (1992).
34. L. F. Brown, B. Berse, R. W. Jackman, K. Tognazzi, E. J. Manseau, D. R. Senger, and H. F. Dvorak, *Cancer Res.* **53,** 4727 (1993).
35. L. Hlatky, C. Tsionou, P. Hahnfeldt, and C. N. Coleman, *Cancer Res.* **54**(23), 6083 (1994).
36. D. Shweiki, M. Neman, A. Itin, and E. Keshet, *Proc. Natl. Acad. Sci.* **92**(3), 768 (1995).
37. M. Toi, S. Hoshina, T. Takayanagi, and T. Tominaga, *Jpn. J. Cancer Res.* **85,** 1045 (1994).
38. L. F. Brown, B. Berse, R. W. Jackman, K. Tognazzi, A. J. Guidi, H. F. Dvorak, D. R. Senger, J. L. Connolly, and S. J. Schnitt, *Human Path.* **26**(1), 86 (1995).
39. H. J. Weinmann, M. Laniado, and W. Mutzel, *Phys. Chem. Phys. Med.* **16,** 167 (1984).